Enhancement mechanisms of sub-bandgap broadband absorption in pyramid-structured silicon

View Online   Export Citation   CrossMark

Zhe Li, Tieyan Zhang, [ID] Jiachen Yu, [ID] Qiqige Wulan, Xiangru Zhou, and Zhijun Liu[a] [ID]

AFFILIATIONS

School of Optoelectronic Science and Engineering, University of Electronic Science and Technology of China, Chengdu, Sichuan 610054, China

[a]Author to whom correspondence should be addressed: liuzhijun@uestc.edu.cn

ABSTRACT

Structure-engineered silicon exhibits a wealth of unique optical properties below its bandgap, which holds promise for mid-infrared and terahertz applications such as photodetection, thermophotovoltaics, radiative cooling, and spectroscopy. In this paper, we investigate enhancement mechanisms of sub-bandgap absorption of black silicon fabricated into periodic pyramids. Our measurements indicate that the pyramid structure leads to an enhanced broadband absorption in the wavelength region from 1.5 to 13.07 μm with an efficiency of over 80%. The broadband absorption enhancement is shown to originate from the Rayleigh–Wood anomaly, localized magnetic plasmonic resonance, and graded-index effect, which together facilitate the interaction between light and free-carriers in silicon. These results are helpful for understanding the interaction between light and black silicon.

Published under an exclusive license by AIP Publishing. https://doi.org/10.1063/5.0062227

I. INTRODUCTION

Silicon, as one of the most efficient and essential semiconductor materials, has attracted persistent interest in studying both fundamental optical phenomena and applied device functionalities. Besides typical above-bandgap applications in photodetectors, solar cells, photocatalytic devices, etc.,[1–3] silicon also exhibits interesting mid-infrared and terahertz properties below its bandgap. As early as in 1967, Satō first observed high emissivity of intrinsic silicon over a wide range of wavelengths from 0.4 to 15 μm at elevated temperatures.[4] Since then, enhanced broadband absorption and thermal emission have been widely reported in black silicon fabricated into various structures such as micro-cones,[5–7] nanopores,[8] nano-needles,[9] and nanowires.[10] In addition, a number of studies have also revealed low reflectivity of visible light and photocarrier recombination dynamics in black silicon, which have great implications for solar energy harvesting.[11,12] Besides black silicon, a variety of special resonant properties from dark mode, toroidal resonance, and bound state in continuum (BIC) have been revealed in silicon metasurfaces fabricated into periodic nano-rods of different shapes.[13–15] Recently, nonlinear supercontinuum generation was

also demonstrated in silicon waveguides, which manifested great potential of silicon for use in spectroscopy.[16,17]

Among sub-bandgap properties of black silicon, broadband mid-infrared absorption has received considerable attention due to its potential use in emerging areas such as infrared sensing, thermal energy harvesting, and radiative cooling.[18–20] The below-bandgap optical response of black silicon is generally related to the elongated light path within random or periodic surface structures, which leads to enhanced interaction between free-carriers and light. Sher *et al.* studied strong absorption of micrometer-sized silicon cones with wavelengths up to 14 μm and attributed sub-bandgap absorption enhancement to multiple light reflections on the cone surface and graded-index profile with reduced reflectance.[21,22] Wang *et al.* further investigated silicon nanocone arrays and revealed that Mie resonance and Rayleigh–Wood anomaly contributed to strong light absorption, especially for the above-bandgap wavelength region.[23] In addition, Gorgulu *et al.* fabricated periodic silicon square patches, and multiple plasmonic resonances were found to contribute to strong broadband sub-bandgap absorption.[24] Recently, Fan *et al.* demonstrated a narrow-band strong

absorption at 0.6 THz in silicon disk arrays, which was attributed to co-excitation of magnetic and electric dipole resonances.[25] In spite of these physical insights on light interaction with surface textured black silicon, our understanding of the enhancement mechanisms of sub-bandgap absorption remains incomplete, which deserve further study due to the complexity of surface morphologies and light–mater interaction on different length scales.

In this paper, we examine mechanisms of light absorption enhancement in periodic pyramid-structured silicon below its bandgap. Silicon pyramids with different sizes and doping concentrations were fabricated to reveal the relationship between light absorbance and structural parameters. Our measurement and theoretical analysis suggest that enhanced broadband absorption below silicon's bandgap originates from Rayleigh–Wood anomaly, localized magnetic plasmonic resonance, and graded-index effect. These results shed light on further understanding the interaction between light and black silicon by taking into account both narrow-band resonances and broadband impedance change.

II. EXPERIMENTS

We used the alkali etching method to fabricate pyramid-structured silicon samples.[26,27] Silicon pyramids of random sizes and positions have been commonly used in solar cells with improved energy conversion efficiency.[28–30] Here, in order to fabricate periodic silicon pyramids, we used a Si_3N_4 mask in the alkali etching process. An 80 nm thick Si_3N_4 layer was first grown on silicon (100) wafer using the plasma enhanced chemical vapor deposition (PECVD) method, and then it was patterned into a disk array by using standard photolithography and dry etching techniques. The sample was next immersed into alkali etching solution made of KOH, IPA, and H_2O with the ratio of 2.891 g:15 ml:50 ml. The etching was conducted at a temperature of 85 °C with an etching time varied between 6 and 15 min. This anisotropic etching preferentially removes more silicon in the (100) plane and less in the (111) plane,[31] leading to the formation of a pyramid with an angle of 54.7° between the two lattice planes of (100) and (111) as illustrated in Fig. 1(a). Finally, the sample was cleaned in phosphorous acid of 85% concentration at 130 °C for removing residue Si_3N_4. To investigate the relationship between surface structure and sub-bandgap absorption of silicon, we fabricated samples with different doping concentrations and pyramid sizes. Pyramid arrays with periods (i.e., base-widths) of P = 2, 3, and 4 μm were made, which correspond to pyramid heights of H = 1.412, 2.118, and 2.825 μm, respectively. Figures 1(b) and 1(c) show top-view and tilted-view scanning electron microscope (SEM) images of a
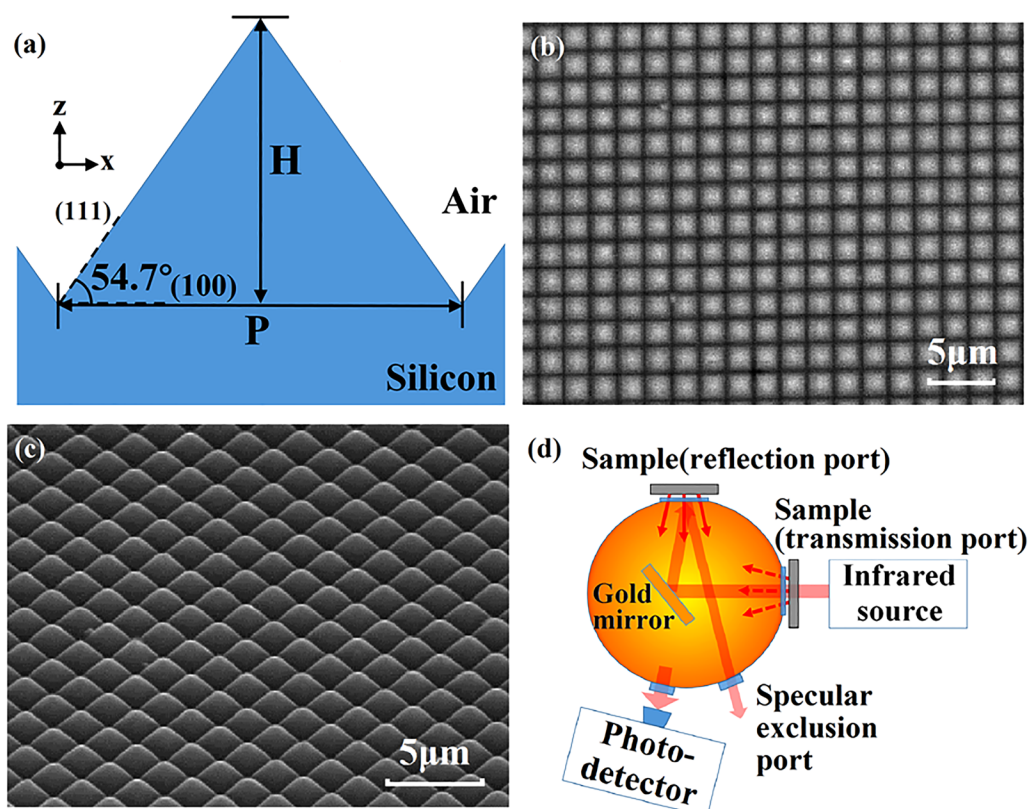

FIG. 1. (a) Schematic of periodic silicon pyramid structure. (b) SEM top-view and (c) tilted-view of a silicon sample with a period of P = 3 μm and a doping level of 2×10^{19} cm^{-3}. (d) is a sketch of the spectral measurement system using an integrating sphere.

representative sample with a period of P = 3 μm and a doping level of 2×10^{19} cm^{-3}. Periodic pyramids with slightly rounded tips were formed with uniform shapes and sizes.

Light absorption of the fabricated silicon samples was characterized with a Fourier transform infrared spectrometer (Nicolet iS50R FTIR) equipped with an upward integrating sphere detector (PIKE Technologies),[32] as sketched in Fig. 1(d). Collimated infrared light from a globar in the FTIR is used as a broadband light source. The inner surface of the integrating sphere is coated with a high reflectance diffuse gold coating, which allows measurements of hemispherical reflection (R$_{total}$) and transmission (T$_{total}$) spectra. Light absorption is obtained as $1 - R_{total} - T_{total}$. In addition, a specular exclusion port is used to include or exclude specular reflection. The difference between R$_{total}$ and diffuse reflection gives the specular reflection spectrum (R$_{spec}$). These hemispherical reflection and transmission measurements include light reflection from the sample substrate back surface.

III. RESULTS AND ANALYSIS

Figure 2(a) shows our measured absorption spectra of pyramid-structured silicon samples with different doping concentrations. The pyramid period is P = 2 μm. We can see that the intrinsic pyramid-structured sample behaves similarly to the intrinsic unetched sample. It exhibits weak absorption within the entire wavelength range of 1.5–17 μm, arising mostly from phonon vibrations.[33] As the doping increases to 1.6×10^{19} cm^{-3}, absorption of the pyramid-structured sample dramatically increases. It exhibits a broadband absorption of about 80% within the band from 1.5 to 13.07 μm. The sharp dip feature at 4.2 μm wavelength is caused by CO_2 absorption in air environment.[34] When the doping increases to 2×10^{19} cm^{-3}, its absorption further increases as shown by the red curve. This strong broadband absorption in doped silicon samples suggests that free-carriers are the main origin of

sub-bandgap absorption, consistent with previous reports.[6,35] In addition, a closer examination of the spectral shape of the two doped samples reveals that the broadband absorption starts to drop at about 14 μm wavelength, which is the plasmon edge effect as reported in our prior work.[36] More importantly, there are two peak features (labeled as "I" and "II") around wavelengths of 2.46 and 6.51 μm, which are likely related to resonances in the pyramid structure.

To study these likely resonance-related properties, we measured absorption spectra of silicon samples with different pyramid sizes. As shown in Fig. 2(b), as the pyramid base-width increases from 2 to 4 μm, the absorption spectrum exhibits an overall increase in magnitude and a frequency shift to the longer wavelengths. Meanwhile, the first absorption peak "I" shifts from 2.46 to 5.1 μm. The second peak "II" shifts from 6.51 to 8.55 μm as the base-width P increases from 2 to 3 μm and becomes barely resolvable for the P = 4 μm sample. These two absorption peak features only exist in the pyramid-structured samples, but not in the unetched sample, which leads us to believe that these two peaks originate from resonant behaviors of the pyramid structure.

In order to understand the measured resonance-related absorption features, we calculated absorption of pyramid-structured silicon using a numerical finite-difference time-domain (FDTD) model. The refractive index of doped silicon was described using the Drude model with relevant carrier parameters given in Refs. 37 and 38. Figure 3 gives permittivity parameters of differently doped silicon used in our model. As the doping concentration increases, the real part of the permittivity ε decreases and changes from positive to negative. Meanwhile, the imaginary part dramatically increases. The heavily doped silicon exhibits metal-like properties in our studied infrared region. Periodic boundary conditions and plane wave excitation were applied in one unit cell of the periodic pyramids for calculating transmission, reflection, and absorption coefficients of the structure. Figure 4(a) shows our calculated absorption spectrum of the sample with a period of P = 2 μm and a
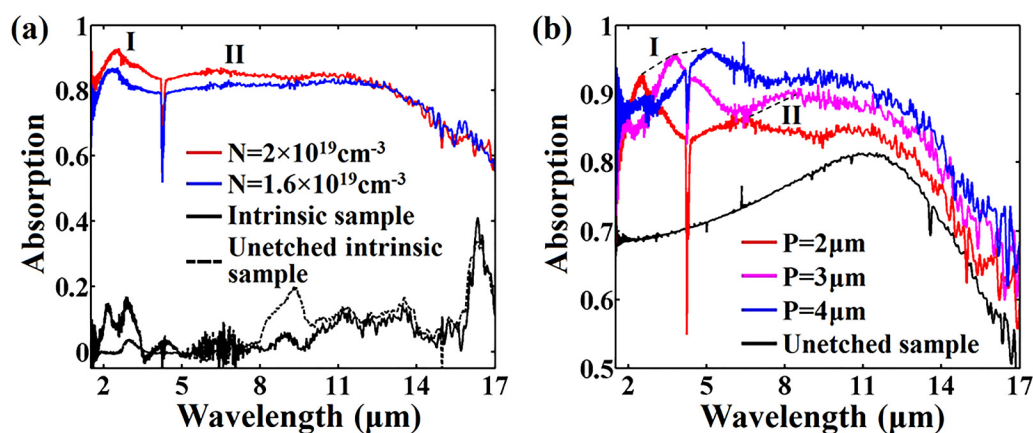

FIG. 2. Measured absorption spectra of (a) pyramid-structured silicon samples with a period of P = 2 μm and different doping concentrations and (b) pyramid-structured silicon samples with a doping concentration of 2×10^{19} cm^{-3} and different periods. The black dashed lines indicate shifts of the peaks "I" and "II" as the pyramid size increases.
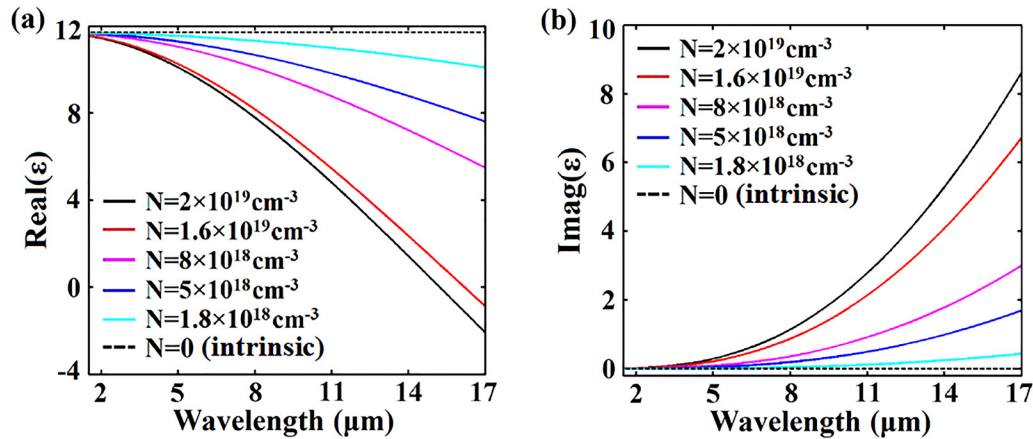
FIG. 3. (a) Real and (b) imaginary parts of permittivity of silicon with different doping concentrations.

doping level of $2 \times 10^{19}\,\mathrm{cm}^{-3}$. The calculated absorption reproduces the main features of the measured result. There is an overall 10% difference in absorption magnitude between calculation and experiment, which likely originates from deviations in material property and pyramid geometry used in the theoretical model. Figure 4(b) shows the calculated absorption spectra of silicon samples with different pyramid sizes. The doping concentration is taken as $2 \times 10^{19}\,\mathrm{cm}^{-3}$. We can see that as the pyramid base-width increases, the two peaks "I" and "II" redshift, which are consistent with those observed behaviors in Fig. 2(b). As these pyramids are periodic, we calculated Rayleigh–Wood anomalies of the structures according to diffraction condition $(\sin\theta + m\lambda/P + n\lambda/P)^2 = 1$,[39] where $\theta = 12°$ is the incident angle, λ is the wavelength, and (m, n) represents the diffraction order. Our calculated wavelengths of (−1,0) Rayleigh–Wood anomalies are marked as arrows in Fig. 4(b), which closely

match positions of the absorption peaks "I." Therefore, we attribute the peak "I" to Rayleigh–Wood anomaly diffraction. It is also noticeable that small oscillations are present on the left shoulder of absorption peak "I" in Fig. 4(b), which are the higher order Rayleigh–Wood anomalies according to calculations. However, these small oscillations are not observed in measured spectra as shown in Fig. 2(b), likely being buried in noise level in the measurement.

For the second peak "II," its wavelength is much larger than the pyramid period. Its calculated field features are shown in Fig. 5. The electrical field is intensified at the pyramid sharp tip. Meanwhile, it forms a vortex within the pyramid, which creates a strong magnetic field as shown in Fig. 5(c). These field features indicate that the absorption peak is related to a magnetic resonance mode in the silicon pyramid. To further verify the plasmonic
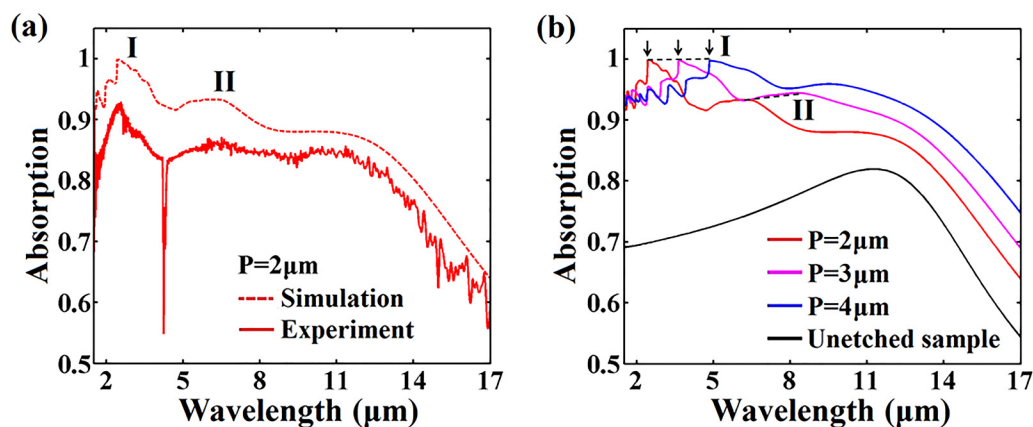

FIG. 4. (a) Comparison between measured and simulated absorption spectra of a pyramid-structured silicon sample with a period of $P = 2\,\mu m$ and a doping level of $2 \times 10^{19}\,\mathrm{cm}^{-3}$. Simulated absorption spectra of the samples with different periods of $P = 2$, 3, and $4\,\mu m$ are shown in (b). The short arrows mark positions of (−1,0) Rayleigh–Wood anomaly. The black dashed lines indicate shifts of the calculated peaks "I" and "II" as the pyramid size increases.
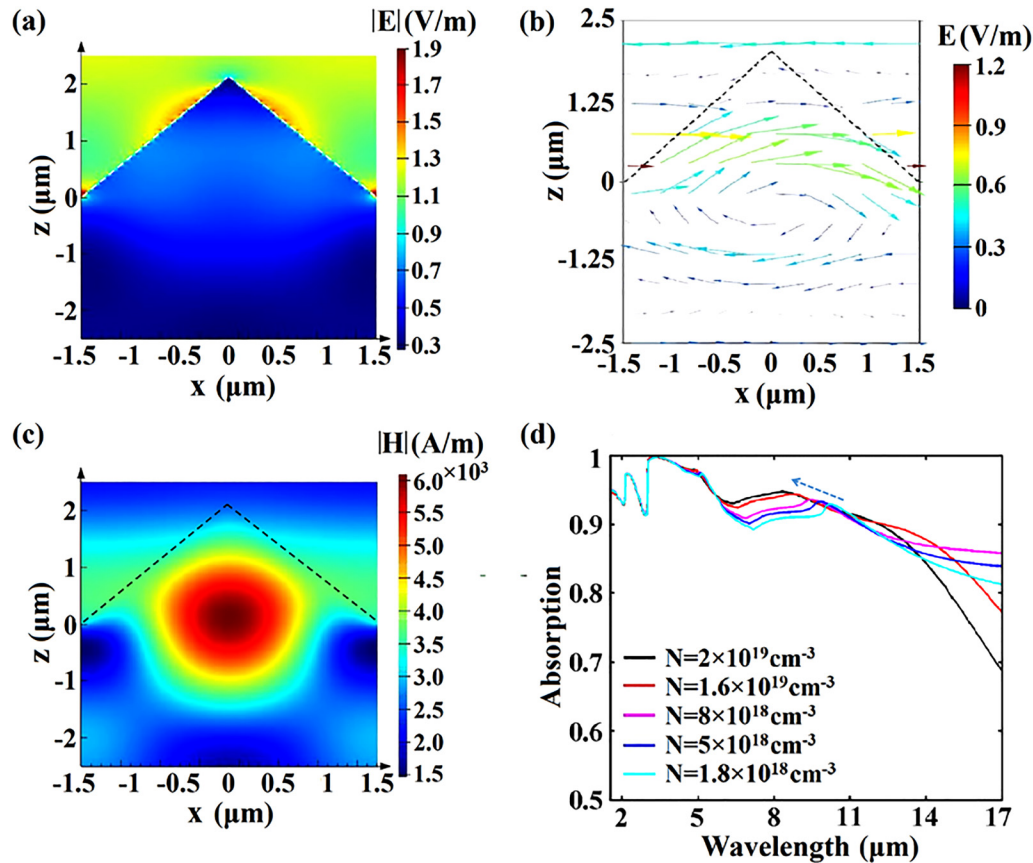
FIG. 5. Simulated (a) electric field intensity, (b) electric field distribution, and (c) magnetic field intensity of localized plasmonic resonance at a wavelength of $8.32 \, \mu m$ for the pyramid-structured sample with a period of $P = 3 \, \mu m$ and a doping level of $N = 2 \times 10^{19} \, cm^{-3}$. (d) shows the calculated absorption spectra of pyramids with different doping levels. The dashed arrow indicates shifts of calculated plasmonic resonance as the doping concentration increases.

nature of this mode, we calculated absorption spectra of the samples with different doping levels as shown in Fig. 5(d). As the doping increases from 1.8×10^{18} to $2 \times 10^{19} \, cm^{-3}$, the resonance absorption peak gradually shifts to shorter wavelengths, as expected for localized plasmonic mode. This blueshift is also observed for the two doped samples of $N = 1.6 \times 10^{19}$ and $2 \times 10^{19} \, cm^{-3}$ as shown in Fig. 2(a).

Besides the above analyzed two resonances, we also notice that the pyramid structure exhibits an overall absorption enhancement outside the resonance region. As shown in Fig. 2(b), as the pyramid size increases from 2 to $4 \, \mu m$, the sample absorption is increased over the wavelength range from 11 to $17 \, \mu m$. We attribute this broadband absorption enhancement to the graded-index effect, which was previously revealed in the structure of silicon nano-tips in Ref. 40. Here, we use effective medium theory to describe such effects in silicon pyramids. As shown in Fig. 6(a), for a representative sample with $P = 3 \, \mu m$ and a doping level of $2 \times 10^{19} \, cm^{-3}$, we divided the pyramid structure into 64 equivalent layers. The effective refractive index of each layer was computed as an average of silicon and air with their volume ratios,[41] namely,

$n_{eff} = [f n_{air}^2 + (1-f) n_{si}^2]^{1/2}$, where n_{air} and n_{si} are the refractive indexes of air and silicon and f is the volume fraction of air. The specular reflection spectrum was then calculated with the transfer matrix method[42] for the equivalent structure with 64 layers and a silicon substrate. To avoid the influence of the above discussed Rayleigh–Wood anomaly and plasmonic mode, we considered the wavelength range between 11 and $17 \, \mu m$ without resonances. Figure 6(b) shows the comparison between calculated and experimental specular reflection spectra for the samples with different pyramid sizes. The calculated spectrum is in excellent agreement with the experiment. The effective refractive index distributions of the sample with $P = 3 \, \mu m$ are shown in Figs. 6(c) and 6(d). It is seen that the indices of the layers at top of the pyramids are close to the index of air and gradually approach that of doped silicon at the bottom of the pyramids. This graded-index effectively couples more light into the structure and enhances light absorption, which is consistent with reduced reflectance as the pyramid size becomes larger as shown in Fig. 6(b). Therefore, for the studied silicon pyramids, both narrow-band resonances and broadband graded-index contribute to the enhanced sub-bandgap absorption.
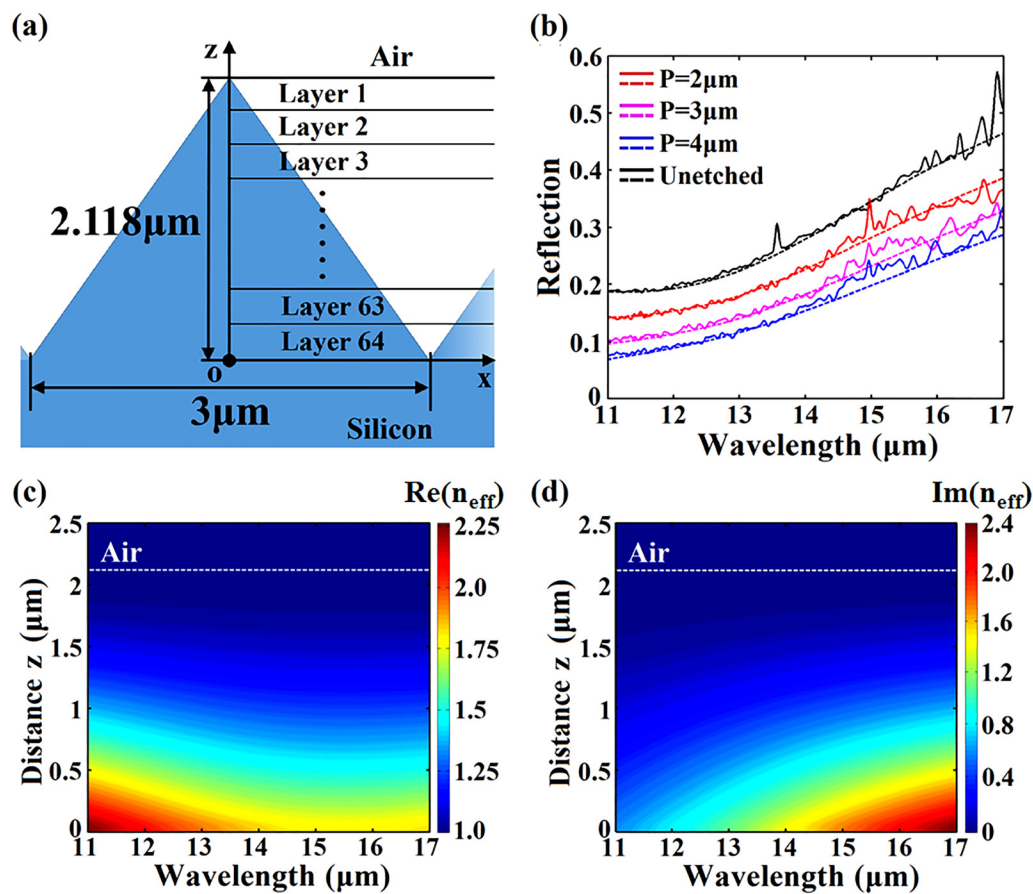
FIG. 6. (a) Schematic of equivalent 64-layers model of pyramid-structured silicon. (b) Comparison of measured (solid curves) and calculated (dashed curves) reflection spectra of the samples with a fixed doping level of 2×10^{19} cm^{-3} and different periods. The black curves are for unetched comparison samples. (c) and (d) give the spatial distribution of the real part and the imaginary part of the effective refractive index of the structure with P = 3 μm. The white dashed lines mark the position of the top tip of the silicon pyramid.

IV. CONCLUSION

We investigated sub-bandgap absorption properties of pyramid-structured silicon in the mid-infrared region. Our spectral measurements on samples with different pyramid sizes and doping concentrations revealed that resonance features exist in silicon's broadband sub-bandgap absorption. Our theoretical calculations and analysis further indicated that besides a broadband graded-index effect, resonances from the Rayleigh–Wood anomaly and localized magnetic plasmonic mode also contribute to enhanced light absorption. These findings add insight for better understanding the enhanced interaction between infrared light and black silicon. We considered periodic silicon pyramids in this work and, for other black silicon structures, their absorption enhancement mechanisms are expected to be similar by considering both non-resonant impedance change and resonant modes, although the resonances are likely to be of a different nature depending on the specific structural geometries.

DATA AVAILABILITY

The data that support the findings of this study are available from the corresponding author upon reasonable request.

REFERENCES

[1]Z. A. F. M. Napiah, R. Gyobu, T. Hishiki, T. Maruyama, and K. Iiyama, IEICE Trans. Electron. **E99.C**, 1304 (2016).

[2]K. Yoshikawa, H. Kawasaki, W. Yoshida, T. Irie, K. Konishi, K. Nakano, T. Uto, D. Adachi, M. Kanematsu, H. Uzu, and K. Yamamoto, Nat. Energy **2**, 17032 (2017).

[3]F. Alexander, M. AlMheiri, P. Dahal, J. Abed, N. S. Rajput, C. Aubry, J. Viegas, and M. Jouiad, Sol. Energy Mater. Sol. Cells **180**, 236 (2018).

[4]T. Satō, Jpn. J. Appl. Phys. **6**, 339 (1967).

[5]C. Wu, C. H. Crouch, L. Zhao, J. E. Carey, R. Younkin, J. A. Levinson, E. Mazur, R. M. Farrell, P. Gothoskar, and A. Karger, Appl. Phys. Lett. **78**, 1850 (2001).

[6]P. G. Maloney, P. Smith, V. King, C. Billman, M. Winkler, and E. Mazur, Appl. Opt. **49**, 1065 (2010).

[7]X. Dong, N. Li, C. Liang, H. Sun, G. Feng, Z. Zhu, H. Shao, X. Rong, L. Zhao, and J. Zhuang, Appl. Phys. Express **6**, 081301 (2013).

[8]H. M. Branz, V. E. Yost, S. Ward, K. M. Jones, B. To, and P. Stradins, Appl. Phys. Lett. **94**, 231121 (2009).

[9]K. Gorgulu, M. Yilmaz, K. Topalli, and A. K. Okyay, J. Opt. **19**, 065101 (2017).

[10]F. Kimeu, S. Albin, K. Song, and K. C. Santiago, AIP Adv. **11**, 065101 (2021).

[11]P. Ščajev, T. Malinauskas, G. Seniutinas, M. D. Arnold, A. Gentle, I. Aharonovich, G. Gervinskas, P. Michaux, J. S. Hartley, E. L. H. Mayes, P. R. Stoddart, and S. Juodkazis, Sol. Energy Mater. Sol. Cells **144**, 221 (2016).

[12]D. Gailevičius, M. Ryu, R. Honda, S. Lundgaard, T. Suzuki, J. Maksimovic, J. Hu, D. P. Linklater, E. P. Ivanova, T. Katkus, V. Anand, M. Malinauskas, Y. Nishijima, S. Hock Ng, K. Staliūnas, J. Morikawa, and S. Juodkazis, Opt. Express **28**, 16012 (2020).

[13]C. Wu, N. Arju, G. Kelp, J. A. Fan, J. Dominguez, E. Gonzales, E. Tutuc, I. Brener, and G. Shvets, Nat. Commun. **5**, 3892 (2014).

[14]Z. F. Sadrieva, I. S. Sinev, K. L. Koshelev, A. Samusev, I. V. Iorsh, O. Takayama, R. Malureanu, A. A. Bogdanov, and A. V. Lavrinenko, ACS Photonics **4**, 723 (2017).

[15]Y. He, G. Guo, T. Feng, Y. Xu, and A. E. Miroshnichenko, Phys. Rev. B **98**, 161112 (2018).

[16]R. K. W. Lau, M. R. E. Lamont, A. G. Griffith, Y. Okawachi, M. Lipson, and A. L. Gaeta, Opt. Lett. **39**, 4518 (2014).

[17]N. Nader, D. L. Maser, F. C. Cruz, A. Kowligy, H. Timmers, J. Chiles, C. Fredrick, D. A. Westly, S. W. Nam, R. P. Mirin, J. M. Shainline, and S. Diddams, APL Photonics **3**, 036102 (2018).

[18]S. I. Woods, J. E. Proctor, T. M. Jung, A. C. Carter, J. Neira, and D. R. Defibaugh, Appl. Opt. **57**, D82 (2018).

[19]Y. X. Yeng, W. R. Chan, V. Rinnerbauer, V. Stelmakh, J. J. Senkevich, J. D. Joannopoulos, M. Soljacic, and I. Čelanović, Opt. Express **23**, A157 (2015).

[20]J.-l. Kou, Z. Jurado, Z. Chen, S. Fan, and A. J. Minnich, ACS Photonics **4**, 626 (2017).

[21]M.-J. Sher, M. T. Winkler, and E. Mazur, MRS Bull. **36**, 439 (2011).

[22]M.-J. Sher, Y.-T. Lin, M. T. Winkler, E. Mazur, C. Pruner, and A. Asenbaum, J. Appl. Phys. **113**, 063520 (2013).

[23]Z. Y. Wang, R. J. Zhang, S. Y. Wang, M. Lu, X. Chen, Y. X. Zheng, L. Y. Chen, Z. Ye, C. Z. Wang, and K. M. Ho, Sci. Rep. **5**, 7810 (2015).

[24]K. Gorgulu, A. Gok, M. Yilmaz, K. Topalli, N. Bıyıklı, and A. K. Okyay, Sci. Rep. **6**, 38589 (2016).

[25]K. Fan, J. Y. Suen, X. Liu, and W. J. Padilla, Optica **4**, 601 (2017).

[26]D. Muñoz, P. Carreras, J. Escarré, D. Ibarz, S. Martín de Nicolás, C. Voz, J. M. Asensi, and J. Bertomeu, Thin Solid Films **517**, 3578 (2009).

[27]J. Jiang, S. Li, Y. Jiang, Z. Wu, Z. Xiao, and Y. Su, J. Mater. Sci. Mater. Electron. **24**, 463 (2013).

[28]E. S. Kolesar, Jr., V. M. Bright, and D. M. Sowders, Thin Solid Films **270**, 10 (1995).

[29]N. Zin, K. McIntosh, S. Bakhshi, A. Vázquez-Guardado, T. Kho, K. Fong, M. Stocks, E. Franklin, and A. Blakers, Sol. Energy Mater. Sol. Cells **183**, 200 (2018).

[30]J. Wang, F. Zhong, H. Liu, L. Zhao, W. Wang, X. Xu, Y. Zhang, and H. Yan, Sol. Energy **221**, 114 (2021).

[31]D. Ananthanarayanan, J. Wong, N. Balaji, A. G. Aberle, and J. W. Ho, Sol. Energy Mater. Sol. Cells **205**, 110286 (2020).

[32]H. Peng, L. Liu, T. Zhang, Z. Li, W. Zhu, J. H. Kim, J. Xu, and Z. Liu, Opt. Mater. Express **9**, 4588 (2019).

[33]R. J. Collins and H. Y. Fan, Phys. Rev. **93**, 674 (1954).

[34]P. A. Gerakines, W. A. Schutte, J. M. Greenberg, and E. F. van Dishoeck, Astron. Astrophys. **296**, 810 (1995).

[35]M. Rüdiger, J. Greulich, A. Richter, and M. Hermle, IEEE Trans. Electron Devices **60**, 2156 (2013).

[36]Z. Li, Y. Zhang, H. Peng, L. Liu, W. Zhu, and Z. Liu, Mater. Res. Express **6**, 126212 (2019).

[37]G. Masetti, M. Severi, and S. Solmi, IEEE Trans. Electron Devices **30**, 764 (1983).

[38]S. Basu, B. J. Lee, and Z. M. Zhang, J. Heat Transf. **132**, 023301 (2010).

[39]H. Gao, J. M. McMahon, M. H. Lee, J. Henzie, S. K. Gray, G. C. Schatz, and T. W. Odom, Opt. Express **17**, 2334 (2009).

[40]Y.-F. Huang, S. Chattopadhyay, Y.-J. Jen, C.-Y. Peng, T.-A. Liu, Y.-K. Hsu, C.-L. Pan, H.-C. Lo, C.-H. Hsu, Y.-H. Chang, C.-S. Lee, K.-H. Chen, and L.-C. Chen, Nat. Nanotechnol. **2**, 770 (2007).

[41]W. Liu, Z. Lai, H. Guo, and Y. Liu, Opt. Lett. **35**, 865 (2010).

[42]K. Ohta and H. Ishida, Appl. Opt. **29**, 1952 (1990).